Polarity-Driven Quasi-3-Fold Composition Symmetry of Self-Catalyzed III−V−V Ternary Core−Shell Nanowires

Yunyan Zhang,*,†,⊥ Ana M. Sanchez,*,‡,⊥ Jiang Wu,†,⊥ Martin Aagesen,§ Jeppe V. Holm,§,‖ Richard Beanland,‡ Thomas Ward,‡ and Huiyun Liu*,†

†Department of Electronic and Electrical Engineering, University College London, London WC1E 7JE, United Kingdom
‡Department of Physics, University of Warwick, Coventry CV4 7AL, United Kingdom
§Gasp Solar ApS, Gregersensvej 7, Taastrup DK-2630, Denmark
‖Center for Quantum Devices, Nano-Science Center, Niels Bohr Institute, University of Copenhagen, Universitetsparken 5, DK-2100 Copenhagen, Denmark

ABSTRACT: A quasi-3-fold composition symmetry has for the first time been observed in self-catalyzed III−V−V core−shell nanowires. In GaAsP nanowires, phosphorus-rich sheets on radial {110} planes originating at the corners of the hexagonal core were observed. In a cross section, they appear as six radial P-rich bands that originate at the six outer corners of the hexagonal core, with three of them higher in P content along ⟨112⟩A direction and others along ⟨112⟩B, forming a quasi-3-fold composition symmetry. We propose that these P-rich bands are caused by a curvature-induced high surface chemical potential at the small corner facets, which drives As adatoms away more efficiently than P adatoms. Moreover, their polarity related P content difference can be explained by the different adatom bonding energies at these polar corner facets. These results provide important information on the further development of shell growth in the self-catalyzed core−shell NW structure and, hence, device structure for multicomponent material systems.

KEYWORDS: III−V−V, ternary, self-catalyzed, GaAsP nanowire, core−shell, polarity, P-rich bands, compositional phase segregation, quasi-3-fold symmetry
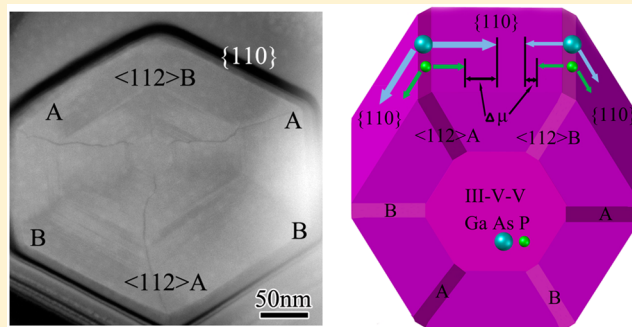
Semiconductor nanowires (NWs) have attracted great attention due to their potential for novel device structures and functionalities.[1−3] The lack of lateral constraint on a nanowire far from the substrate allows it to readily adopt an unstrained lattice parameter, while its small size renders dislocations unstable, producing dislocation-free material.[4−6] This allows materials with a large lattice and thermal expansion coefficient mismatch, such as III−Vs and Si, to be monolithically integrated, which is a goal pursued for more than 40 years.[7−11] Furthermore, NWs often possess novel crystallographic,[12,13] photonic,[14−16] electric,[17,18] and mechanical[19] properties that do not occur in thin film structures, which may allow the development of disruptive technologies in a wide range of fields[20−24] with rather different approaches to device design compared with traditional thin film devices.[25−33] In order to make good use of those merits, radial core−shell geometries are particularly important due to their band structures and engineering functionality.[34] Core−shell NWs have been useful for a variety of applications, ranging from NW emitters to NW photovoltaic devices.[35−38]

Ternary and quaternary III−V semiconductors provide large composition tunability and, hence, bring flexibility to the design of core−shell strain and band structure. However, the nonplanar surface of the NW and the property differences of elements make the multicomponent shell growth more complex. The curvature of the outer surface of the NWs can change the surface chemical potential and, hence, affect the diffusion properties of adatoms.[39−41] The phase segregation has been reported in III−III−V core−shell ternary NWs. In particular, the corner regions of NWs with multicomponent shells are commonly observed to have compositional phase segregation. For example, Al-rich bands have been observed in the transmission electron microscope (TEM) cross sections of both ternary $AlIn_yP_{1−y}$[40,42] and $Al_xGa_{1−x}As$[43−47] ⟨111⟩ NWs, originating from the six outer corners of the core and extending radially along ⟨112⟩ directions to the outer vertices of the shell. This phase segregation has recently been found to have a 3-fold symmetry that is determined by the crystal polarity.[44,48] These compositional inhomogeneities can change the local properties, such as band structure, doping efficiency, and the strain, which will affect carrier effective mass, transportation, and hence degrade device performance. On the other hand, the control of
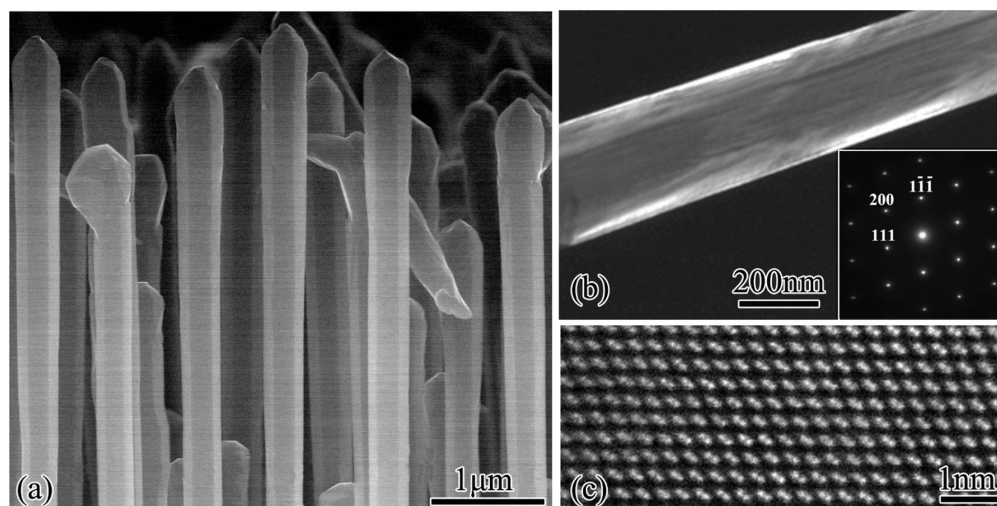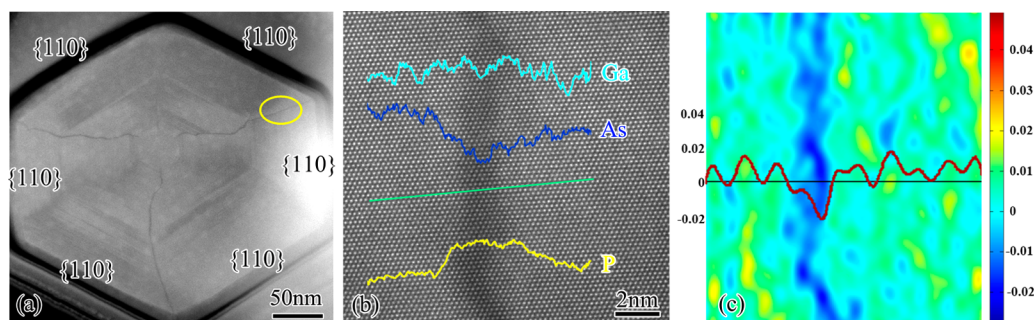
Figure 1. (a) Side-view SEM image of the core−shell $GaAs_{0.8}P_{0.2}$ NWs. (b) Conventional DF-TEM image and the diffraction pattern of a $GaAs_{0.8}P_{0.2}$ core−shell NW. (c) High-magnification annular dark field image of the NW shown in (b).
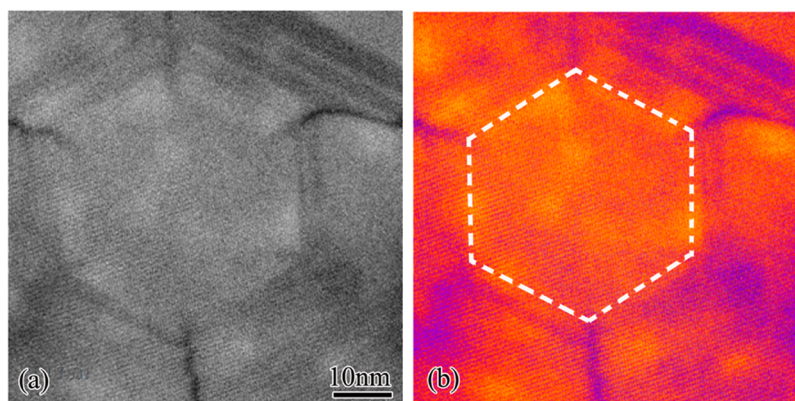

Figure 2. (a) ADF-STEM image of the core−shell NW cross section. (b) High-resolution ADF-STEM of the area in the yellow ellipse in (a), containing a dark band. An X-ray count profile along the green line is overlaid. (c) Strain along the horizontal axis, ε_{xx}, of the location encompassing (b), as measured by the geometric phase algorithm. A line profile is overlaid.

these effects can lead to new device geometries. For example, it has been demonstrated that AlGaAs quantum dots (QDs) can be formed in NWs by phase segregation,[49] without the assistance of the strain, which is different to QDs obtained via the Stranski−Krastanow growth mode.[50] This quantum dot fabrication method offers more freedom in band structure engineering and device structure design. It is therefore of great importance to investigate variations in the composition of NWs and the underlying mechanisms that produce them, giving control and avoiding their potential adverse effects. Although phase segregation in III−V−V core NWs was demonstrated recently,[51−53] there is no report on phase segregation for III−V−V core−shell NWs in the literature. More research on the III−V−V shell growth, thus, is imperative.

In this Letter, we have systematically studied core−shell $GaAs_yP_{1-y}$ NWs by scanning electron microscopy (SEM), annular dark field scanning TEM (ADF-STEM) and convergent beam electron diffraction (CBED). In cross section, six P-rich bands, originating at the outer corners of the hexagonal core and extending radially along $\langle 112 \rangle$ directions to the outer vertices of shell are present. The three bands along $\langle 112 \rangle$A directions have higher P-content than others along $\langle 112 \rangle$B, forming a quasi-3-fold compositional distribution. It is proposed that adatom bonding energy and facet polarity are key parameters that influence this phase segregation.

The $GaAs_yP_{1-y}$ NWs were grown on 380 μm thick p-doped silicon (111) substrates with a thin layer of native oxide by a solid-source molecular beam epitaxy. The core NWs were grown by Ga-catalyzed vapor−liquid−solid (VLS) growth mode.[54] The beam equivalent pressures of Ga, As, P flux were 8.72×10^{-8}, 3.07×10^{-6} and 4.2×10^{-7} Torr, respectively. The substrate temperature was kept at ∼640 °C as measured by a pyrometer for the growth of core $GaAs_{0.8}P_{0.2}$ nanowires. After the growth of the nanowire cores, the Ga droplets were crystallized into GaAsP by closing the Ga shutter and supplying As and P flux at 6.9×10^{-6} and 3.1×10^{-6} Torr, respectively. Subsequent the shell growth was carried out by reopening the Ga flux at the substrate temperatures between 460 and 470 °C. The nominal structure is a $GaAs_{0.8}P_{0.2}$ core with a shell of the same composition. Further details can be found elsewhere.[20,55,56] The NW morphology was measured by a JEOL-JSM-6320F SEM. Simple scraping of NWs onto a lacey carbon support was used to prepare TEM specimens for complete NWs, whereas a focused ion beam (FIB) lift-out technique was employed to prepare cross section specimens using a JEOL 4500 FIB/SEM. The TEM measurement was performed on JEOL 2100 and doubly corrected ARM200F microscopes, both operating at 200 kV. Compositional analysis using energy-dispersive X-ray spectrometry (EDX) was performed using Oxford Instruments 80 mm^2 SDD EDX detectors.

Figure 3. (a) ADF-STEM image at the center of the NW cross section. (b) False color image of (a). White dashed lines indicate the core area.
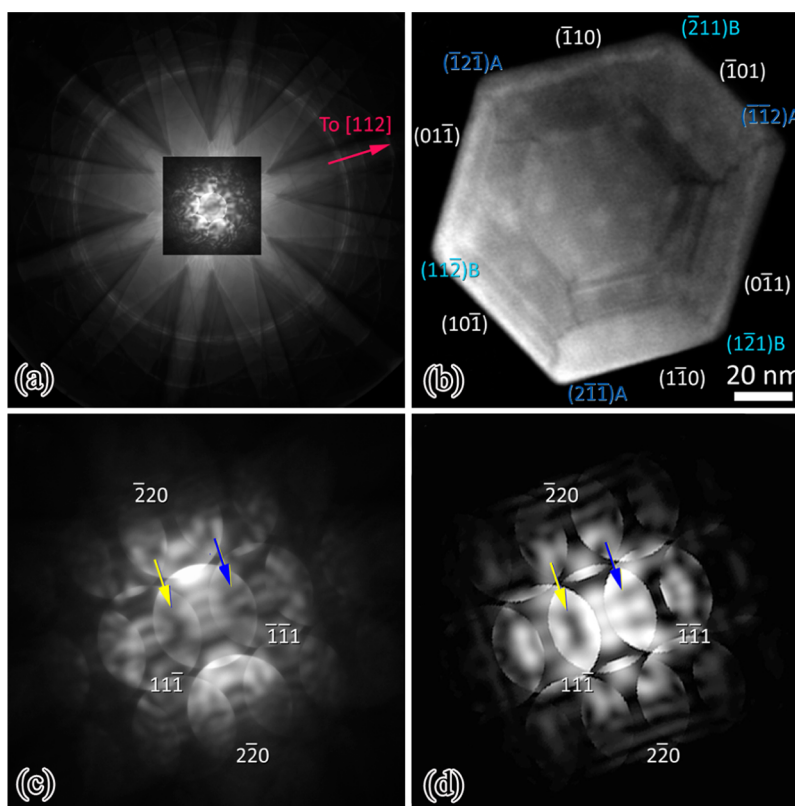
Figure 4. (a) Kikuchi pattern and [111] CBED pattern (inset) recorded with the electron beam along the nanowire growth direction. (b) ADF-STEM image of the core−shell NW marked with the sidewall polarities. (c) [112] CBED pattern (d) Simulated [112] CBED pattern for $GaAs_{0.8}P_{0.2}$ at a specimen thickness of 75 nm. Bright and dark features in the polarity-sensitive 111-type discs are marked with arrows in (c) and (d).

Figure 1a shows a SEM image of the core−shell NWs. Each NW has a relatively uniform diameter along the growth direction and smooth side facets. Previously, we have shown that the defects of the core NW are concentrated at the very tip and bottom, whereas the body of the NW is almost defect-free with only a few single twin planes.[56] Because the core NW acts as a substrate for epitaxy growth of the shell, the crystal structure is extended to shell. As can be seen in the dark field TEM and ADF-STEM images of Figure 1b and c, the shell has the same cubic (zincblende) crystal structure as the core, which is also evident in the diffraction pattern in the inset of Figure 1b. Twins are so sparse that the segment in Figure 1b is completely defect-free. Figure 1c shows a magnified ADF-STEM image of a representative section of the NW with pure zincblende structure and free of twins.

In order to investigate the composition distribution inside the core−shell NWs, FIB/SEM cross sections were prepared (thickness ∼70 nm) and examined using STEM. As can be seen in Figure 2a, the NW has an approximate hexagonal cross section with three distinct meandering dark radial bands running from close to the center to alternate outer vertices of the NW (the junctions between {110} side faces) and forming a quasi-3-fold symmetry. The irregular hexagonal shape of the NWs can be explained by the random nucleation of the self-catalyzed NWs that compete for the Ga adatoms with its adjacent wires. The distance between the NWs is random and, thus, the supply of Ga atoms to each facet of the NWs is anisotropic. Three indistinct dark radial bands are also present between them, terminating at the other NW outer vertices. In addition, sharp, straight, bright and dark bands and blocks of

material, with edges parallel to the side faces of the NW are also present. However, their formation mechanism is unclear and under further study. ADF-STEM contrast is proportional to an exponent of the atomic number Z^m, $m \sim 1.6$ to 2. Thus, Figure 2a may be interpreted as variations in the As/P ratio of the material, with bright regions corresponding to high As content and dark regions to high P content. This is confirmed by the EDX line profile in Figure 2c, which shows that dark bands are rich in P (and deficient in As) in comparison with the adjacent brighter material, with a difference of the order of 10 atomic %. Furthermore, an analysis of the ADF-STEM image by the geometric phase algorithm (Figure 2c) indicates that the dark bands have a smaller interatomic spacing, consistent with higher P content ($GaAs_{0.6}P_{0.4}$ has a lattice parameter of 0.55573 nm, whereas $GaAs_{0.8}P_{0.2}$ has a lattice parameter of 0.5613 nm, i.e., a difference of 0.7%). Clearly, compositional phase segregation has occurred during growth of the GaAsP shell.

A higher magnification image of the NW core is shown in Figure 3a, in which the composition variations can be seen more clearly. The central part of the NW indicated in Figure 3b (~50 nm diameter) is a regular hexagon with uniform composition, which is consistent with the NW core grown at high temperature with VLS growth mode. The three distinct P-rich dark bands shown in Figure 2a are found originate at the outer corners of this hexagonal core and run to the outer vertices of the shell. In the NW, which is a 3-dimensional hexagonal prism, these bands correspond to P-rich planes, linking the corners of core and shell. Furthermore, the three comparatively indistinct dark bands can also be seen to originate from the other three corners. These additional bands are not as dark, indicating a lower P content compared with the dark P-rich bands.

Although the NWs have a hexagonal section, the material is cubic and a 3-fold symmetry is entirely consistent with this. Furthermore, because the material is noncentrosymmetric, there is in general a physical difference between surfaces with opposite orientations (h k l) and ($-h$ $-k$ $-l$). They will be terminated with group III cations in one case and group V anions in the other. This is often referred to as A and B polarity.[57] However, some surfaces contain equal numbers of cations and anions and are neutral, or nonpolar. These tend to have low energies and the {110} side faces are an example of this. Nevertheless, the corners that lie between adjacent {110} faces (or small {211} facets that may form there[44]) are polar, and different growth mechanisms and incorporation rates may be expected.

The polarity of the side facets can be determined using convergent beam electron diffraction (CBED), as shown in Figure 4. Figure 4a shows the Kikuchi pattern and CBED pattern (inset) with the electron beam along the nanowire growth direction [111], whereas Figure 4b shows the NW section aligned to the diffraction pattern. Simulations of the [111] CBED pattern using JEMS showed that the contrast in the polarity-sensitive 224 discs changed considerably as a function of composition and specimen thickness, which would give difficulties in interpretation. However, simulations of the [112] pattern showed consistent bright/dark contrast in the polarity-sensitive 11−1 and −1−11 discs (arrowed, Figure 4d) for all compositions and a wide range of thicknesses. The sample was thus tilted to the [112] zone axis following the 220 Kikuchi lines and a CBED pattern was obtained (Figure 4c). The bright/dark contrast in the 111-type discs allows unambiguous indexing of the [112] and [111] patterns, and

in turn the absolute orientation of the NW section (Figure 4b). Therefore, it can be identified that the distinct P-rich bands run from the core toward ⟨112⟩A directions, whereas the indistinct bands are in ⟨112⟩B directions. In order to understand this phenomenon, it is necessary to understand the mechanism behind the formation of P-rich bands.

In general, surfaces with high symmetry (low Miller index facets) have low surface energy. Therefore, NWs are normally observed to be bounded by {110} and {112} side facets due to their low surface energy.[44] It has been suggested that the surface energy of the {112} plane is at least three times that of the {110} plane.[57] The difference in the surface energy gives an anisotropy in the growth rate, making the high Miller index facets grow faster. Therefore, {112} facets grow faster than {110} facets and become smaller. As a result, the core−shell NW has {110} facets with convex corners where {110} facets meet, as shown schematically in Figure 5. On the other hand,
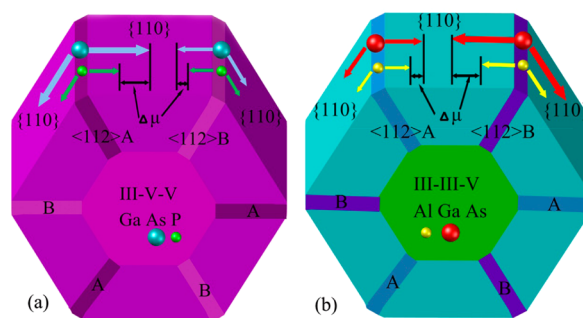
Figure 5. Illustrations of (a) III−V−V and (b) III−III−V type core−shell NW phase segregation mechanism.

when the {112} facets get smaller, their effective curvature increases, which can raise the surface chemical potential relative to the {110} facets.[41] Therefore, the surface chemical potential difference can drive the adatoms to diffuse from the high chemical potential {112} facets to the low chemical potential {110} facets, forming a capillary flux.[40] This will decrease the growth rate on {112} facets. Eventually, the counteracting effects of the surface energy and the chemical potential will produce a self-limited balance in the {112} facet growth rate. For the multicomponent material, the different elements have different cohesive energies (chemical bonding energy) with the substrate surface,[58] which leads to different diffusion coefficients (diffusion length).[59] When growing a multicomponent shell, as illustrated in Figure 5, the ⟨112⟩ directions are commonly observed to be rich in the elements with stronger bonding and shorter diffusion length because the elements with lower bonding energy will diffuse away more easily. Due to the strong chemical bonding energy of GaP compared with that of GaAs,[58] the diffusion length of the P adatom is shorter than that of As. Therefore, more As atoms can diffuse away from the {112} facets and leave P rich bands along the ⟨112⟩ directions.

As discussed above, the 3-fold symmetry of the P-rich bands are connected with the side facet polarities. Because the {110} facets are nonpolar and all equal, the cause of the 3-fold symmetry formation should be the {112} facets. As seen in Table 1, the {112}A facets have two 3-fold-coordinated group-III atoms and one 2-fold-coordinated group-V surface atom in each 1 × 1 unit cell, whereas the {112}B facets have two 3-fold-coordinated group-V atoms and one 2-fold-coordinated group-

Table 1. Surface Adatom Bond Information on {112}A and B Facets in Each 1 × 1 Unit Cell[57]

{112} facet	group III atoms bonding site			group V atoms bonding site		
	bond type	site number	bond strength	bond type	site number	bond strength
A	3-fold-coordinated	2	strong	2-fold-coordinated	1	weak
B	2-fold-coordinated	1	weak	3-fold-coordinated	2	strong

III atom per 1 × 1 unit cell.[57] Therefore, two (three) new bonds are formed for every incoming group-V (group-III) atom for the {112}A facets, whereas three (two) new bonds are formed for the {112}B sidewalls.[48,60,61] This makes the group-V (group-III) atoms have much stronger bonds at the {112}B ({112}A) facets. As a result, the group-V (group-III) adatoms have larger incorporation coefficients on {112}B ({112}A) facets, which leads to weaker compositional phase segregation compared with the facets of opposite polarity. In the GaAsP shell, as illustrated in Figure 5a, the polarity-related surface features can significantly affect the diffusion length of As (μ_{As}), the diffusion length of P (μ_P), and the difference between them $\Delta\mu_{AsP} = (\mu_{As} - \mu_P)$, which can in turn influence the diffused-away adatom flux of As (n_{As}), the diffused-away adatom flux of P (n_P), and the difference between them $\Delta n_{AsP} = (n_{As} - n_P)$. At the {112}B ({112}A) facets, the As and P adatoms have stronger (weaker) bonding energy, which makes the $\Delta\mu_{AsP}$ become smaller (larger). This can reduce (increase) Δn_{AsP}. Therefore, it will lead to weaker (stronger) element selectivity and lower (stronger) compositional phase segregation. In the end, the ⟨112⟩A direction P-rich bands have higher P content than those along the B directions.

In summary, we have observed the compositional phase segregation for the first time in the shell of III–V–V ternary NWs by studying the GaAsP core–shell NWs, shown as P-rich bands along the six ⟨112⟩ directions in the cross section. They initiate at the outer corners of the core and extend radially to reach the outer vertices of the shell. This phenomenon is explained by the curvature-induced high surface chemical potential at the small {112} facets, which drives away the longer diffusion length element (As) more efficiently. Moreover, the six P-rich bands can be divided into two groups with different P content. Due to the alternating arrangement of the two types of bands about the NW axis, they are found to have a quasi-3-fold symmetry. The three bands with higher P content are along ⟨112⟩A directions and those with a lower P content are along ⟨112⟩B. This polarity-driven symmetry is proposed to be due to the stronger (weaker) bonding energy of {112}B ({112}A) facets with the group-V adatoms, which can reduce (increase) the diffusion length difference between As and P. These results could provide important information for further developing the multicomponent core–shell NW growth.

AUTHOR INFORMATION

Corresponding Authors

*E-mail: yunyan.zhang.11@ucl.ac.uk.
*E-mail: a.m.sanchez@warwick.ac.uk.
*E-mail: huiyun.liu@ucl.ac.uk.

Author Contributions

[⊥]Y.Z., A.S., and J.W. contributed equally to this work.

Notes

The authors declare no competing financial interest.

REFERENCES

(1) Yang, P.; Yan, R.; Fardy, M. *Nano Lett.* **2010**, *10*, 1529.
(2) Yan, R.; Gargas, D.; Yang, P. *Nat. Photonics* **2009**, *3*, 569.
(3) Lieber, C. M.; Wang, Z. L. *MRS Bull.* **2007**, *32*, 99.
(4) Ertekin, E.; Greaney, P. A.; Chrzan, D. C.; Sands, T. D. *J. Appl. Phys.* **2005**, *97*, 114325.
(5) Larsson, M. W.; Wagner, J. B.; Wallin, M.; Håkansson, P.; Fröberg, L. E.; Samuelson, L.; Wallenberg, L. R. *Nanotechnology* **2007**, *18*, 015504.
(6) Ercolani, D.; Rossi, F.; Li, A.; Roddaro, S.; Grillo, V.; Salviati, G.; Beltram, F.; Sorba, L. *Nanotechnology* **2009**, *20*, 505605.
(7) Mathine, D. L. *IEEE J. Sel. Top. Quantum Electron.* **1997**, *3*, 952.
(8) Roelkens, G.; Liu, L.; Liang, D.; Jones, R.; Fang, A.; Koch, B.; Bowers, J. *Laser Photonics Rev.* **2010**, *4*, 751.
(9) Lee, A.; Liu, H.; Seeds, A. *Semicond. Sci. Technol.* **2013**, *28*, 015027.
(10) Wang, T.; Liu, H.; Lee, A.; Pozzi, F.; Seeds, A. *Opt. Express* **2011**, *19*, 11381.
(11) Lee, A. D.; Qi, J.; Tang, M.; Zhang, Y.; Seeds, A. J.; Liu, H. *IEEE J. Sel. Top. Quantum* **2013**, *19*, 1701510.
(12) Caroff, P.; Dick, K. A.; Johansson, J.; Messing, M. E.; Deppert, K.; Samuelson, L. *Nat. Nanotechnol.* **2008**, *4*, 50.
(13) Assali, S.; Zardo, I.; Plissard, S.; Kriegner, D.; Verheijen, M. A.; Bauer, G.; Meijerink, A.; Belabbes, A.; Bechstedt; Haverkort, J. E. M.; Bakkers, E. P. A. M. *Nano Lett.* **2013**, *13*, 1559.
(14) Wilhelm, C.; Larrue, A.; Dai, X.; Migas, D.; Soci, C. *Nanoscale* **2012**, *4*, 1446.
(15) Scofield, A. C.; Kim, S.-H.; Shapiro, J. N.; Lin, A.; Liang, B.; Scherer, A.; Huffaker, D. L. *Nano Lett.* **2011**, *11*, 5387.
(16) Lopez, F. J.; Hemesath, E. R.; Lauhon, L. J. *Nano Lett.* **2009**, *9*, 2774.
(17) Parkinson, P.; Joyce, H. J.; Gao, Q.; Tan, H. H.; Zhang, X.; Zou, J.; Jagadish, C.; Herz, L. M.; Johnston, M. B. *Nano Lett.* **2009**, *9*, 3349.
(18) Wallentin, J.; Ek, M.; Wallenberg, L. R.; Samuelson, L.; Borgström, M. T. *Nano Lett.* **2011**, *12*, 151.
(19) Bao, P.; Wang, Y.; Cui, X.; Gao, Q.; Yen, H.; Liu, H.; Yeoh, W. K.; Liao, X.; Du, S.; Tan, H. H.; Jagadish, C.; Zou, J.; Ringer, S. P.; Zheng, R. *Appl. Phys. Lett.* **2014**, *104*, 021904.
(20) Wu, J.; Li, Y.; Kubota, J.; Domen, K.; Aagesen, M.; Ward, T.; Sanchez, A.; Beanland, R.; Zhang, Y.; Tang, M.; Hatch, S.; Seeds, A.; Liu, H. *Nano Lett.* **2014**, *14*, 2013.
(21) LaPierre, R. R. *J. Appl. Phys.* **2011**, *110*, 014310.
(22) Wu, J.; Zhang, Y.; Tutu, F.; Lam, P.; Hatch, S.; Liu, H. *J. Opt. Soc. Am.* **2013**, RM1D–1.
(23) Nguyen, H. P. T.; Zhang, S.; Connie, A. T.; Kibria, M. G.; Wang, Q.; Shih, I.; Mi, Z. *Nano Lett.* **2013**, *13*, 5437.
(24) Krogstrup, P.; Jørgensen, H. I.; Heiss, M.; Demichel, O.; Holm, J. V.; Aagesen, M.; Nygard, J.; i Morral, A. F. *Nat. Photonics* **2013**, *7*, 306.
(25) Zhang, Y. Y.; Yin, Y. A. *Appl. Phys. Lett.* **2011**, *99*, 221103.
(26) Zhang, Y. Y.; Fan, G. H.; Yin, Y. A.; Yao, G. R. *Opt. Express* **2012**, *20*, A133.
(27) Yun-Yan, Z.; Guang-Han, F. *Chin. Phys. B* **2011**, *20*, 048502.
(28) Zhang, Y. Y.; Yao, G. R. *J. Appl. Phys.* **2011**, *110*, 093104.

(29) Nguyen, H. P. T.; Cui, K.; Zhang, S.; Djavid, M.; Korinek, A.; Botton, G. A.; Mi, Z. *Nano Lett.* **2012**, *12*, 1317.

(30) Ra, Y. H.; Navamathavan, R.; Park, J. H.; Lee, C. R. *Nano Lett.* **2013**, *13*, 3506.

(31) Zhao, S.; Fathololoumi, S.; Bevan, K. H.; Liu, D. P.; Kibria, M. G.; Li, Q.; Wang, G. T.; Guo, H.; Mi, Z. *Nano Lett.* **2012**, *12*, 2877.

(32) Kuykendall, T.; Ulrich, P.; Aloni, S.; Yang, P. *Nat. Mater.* **2007**, *6*, 951.

(33) Dasgupta, N. P.; Sun, J.; Liu, C.; Brittman, S.; Andrews, S. C.; Lim, J.; Gao, H.; Yan, R.; Yang, P. *Adv. Mater.* **2014**, *26*, 2137.

(34) Lauhon, L. J.; Gudiksen, M. S.; Wang, D.; Lieber, C. M. *Nature* **2002**, *420*, 57.

(35) Qian, F.; Li, Y.; Gradečak, S.; Park, H. G.; Dong, Y.; Ding, Y.; Wang, Z. L.; Lieber, C. M. *Nat. Mater.* **2008**, *7*, 701.

(36) Sköld, N.; Karlsson, L. S.; Larsson, M. W.; Pistol, M. E.; Seifert, W.; Trägårdh, J.; Samuelson, L. *Nano Lett.* **2005**, *5*, 1943.

(37) Couto, O., Jr.; Sercombe, D.; Puebla, J.; Otubo, L.; Luxmoore, I. J.; Sich, M.; Elliott, T. J.; Chekhovich, E. A.; Wilson, L. R.; Skolnick, M. S.; Liu, H. Y.; Tartakovskii, A. I. *Nano Lett.* **2012**, *12*, 5269.

(38) Xiang, J.; Lu, W.; Hu, Y.; Wu, Y.; Yan, H.; Lieber, C. M. *Nature* **2006**, *441*, 489.

(39) Steinke, L.; Cantwell, P.; Zakharov, D.; Stach, E.; Zaluzec, N. J.; i Morral, A. F.; Bichler, M.; Abstreiter, G.; Grayson, M. *Appl. Phys. Lett.* **2008**, *93*, 193117.

(40) Wagner, J. B.; Sköld, N.; Reine Wallenberg, L.; Samuelson, L. *J. Cryst. Growth* **2010**, *312*, 1755.

(41) Mullins, W. W. *J. Appl. Phys.* **1957**, *28*, 333.

(42) Sköld, N.; Wagner, J. B.; Karlsson, G.; Hernán, T.; Seifert, W.; Pistol, M. E.; Samuelson, L. *Nano Lett.* **2006**, *6*, 2743.

(43) Jiang, N.; Gao, Q.; Parkinson, P.; Wong-Leung, J.; Mokkapati, S.; Breuer, S.; Tan, H. H.; Zheng, C. L.; Etheridge, J.; Jagadish, C. *Nano Lett.* **2013**, *13*, 5135.

(44) Zheng, C.; Wong-Leung, J.; Gao, Q.; Tan, H. H.; Jagadish, C.; Etheridge, J. *Nano Lett.* **2013**, *13*, 3742.

(45) Fickenscher, M.; Shi, T.; Jackson, H. E.; Smith, L. M.; Yarrison-Rice, J. M.; Zheng, C.; Miller, P.; Etheridge, J.; Wong, B. M.; Gao, Q.; Deshpande, S.; Tan, H. H.; Jagadish, C. *Nano Lett.* **2013**, *13*, 1016.

(46) Rudolph, D.; Funk, S.; Döblinger, M.; Morkötter, S.; Hertenberger, S.; Schweickert, L.; Becker, J.; Matich, S.; Bichler, M.; Spirkoska, D.; Zardo, I.; Finley, J. J.; Abstreiter, G.; Koblmüller, G. *Nano Lett.* **2013**, *13*, 1522.

(47) Kauko, H.; Zheng, C. L.; Zhu, Y.; Glanvill, S.; Dwyer, C.; Munshi, A. M.; Fimland, B. O.; van Helvoort, A. T. J.; Etheridge, J. *Appl. Phys. Lett.* **2013**, *103*, 232111.

(48) Guo, Y. N.; Burgess, T.; Gao, Q.; Tan, H. H.; Jagadish, C.; Zou, J. *Nano Lett.* **2013**, *13*, 5085.

(49) Heiss, M.; Fontana, Y.; Gustafsson, A.; Wüst, G.; Magen, C.; O'Regan, D. D.; Luo, J. W.; Ketterer, B.; Conesa-Boj, S.; Kuhlmann, A. V.; Houel, J.; Russo-Averchi, E.; Morante, J. R.; Cantoni, M.; Marzari, N.; Arbiol, J.; Zunger, A.; Warburton, R. J.; i Morral, A. F. *Nat. Mater.* **2013**, *12*, 439.

(50) Liu, H. Y.; Sellers, I. R.; Badcock, T. J.; Mowbray, D. J.; Skolnick, M. S.; Groom, K. M.; Gutierrez, M.; Hopkinson, M.; Ng, J. S.; David, J. P. R.; Beanland, R. *Appl. Phys. Lett.* **2004**, *85*, 704.

(51) Conesa-Boj, S.; Kriegner, D.; Han, X. L.; Plissard, S.; Wallart, X.; Stangl, J.; i Morral, A. F.; Caroff, P. *Nano Lett.* **2014**, *14*, 326.

(52) Xu, T.; Dick, K. A.; Plissard, S.; Nguyen, T. H.; Makoudi, Y.; Berthe, M.; Nys, J.; Wallart, X.; Grandidier, B.; Caroff, P. *Nanotechnology* **2012**, *23*, 095702.

(53) Sun, W.; Huang, Y.; Guo, Y.; Liao, Z. M.; Gao, Q.; Tan, H. H.; Jagadish, C.; Liao, X. Z.; Zou, J. *J. Mater. Chem. C* **2015**, *3*, 1745.

(54) Wagner, R. S.; Ellis, W. C. *Appl. Phys. Lett.* **1964**, *4*, 89.

(55) Holm, J. V.; Jørgensen, H. I.; Krogstrup, P.; Nygård, J.; Liu, H.; Aagesen, M. *Nat. Commun.* **2013**, *4*, 1498.

(56) Zhang, Y.; Aagesen, M.; Holm, J. V.; Jørgensen, H. I.; Wu, J.; Liu, H. *Nano Lett.* **2013**, *13*, 3897.

(57) Chadi, D. J. *J. Vac. Sci. Technol., B: Microelectron. Process. Phenom.* **1985**, *3*, 1167.

(58) Paulus, B.; Fulde, P.; Stoll, H. *Phys. Rev. B* **1996**, *54*, 2556.

(59) Kley, A.; Ruggerone, P.; Scheffler, M. *Phys. Rev. Lett.* **1997**, *79*, 5278.

(60) Paladugu, M.; Zou, J.; Guo, Y. N.; Zhang, X.; Joyce, H. J.; Gao, Q.; Tan, H. H.; Jagadish, C.; Kim, Y. *Appl. Phys. Lett.* **2008**, *93*, 201908.

(61) Zou, J.; Paladugu, M.; Wang, H.; Auchterlonie, G. J.; Guo, Y. N.; Kim, Y.; Gao, Q.; Joyce, H. J.; Tan, H. H.; Jagadish, C. *Small* **2007**, *3*, 389.